Evaluation of Methods for Molecular Dynamics Simulation of Ionic Liquid Electric Double Layers

Justin B. Haskins[1] and John W. Lawson[2]
[1)] *AMA Inc., Thermal Protection Materials Branch, NASA Ames Research Center, MS N234-1, Moffett Field, California 94035, USA*[a)]
[2)] *Thermal Protection Materials Branch, NASA Ames Research Center, MS N234-1, Moffett Field, California 94035, USA*

We investigate how systematically increasing the accuracy of various molecular dynamics modeling techniques influences the structure and capacitance of ionic liquid electric double layers (EDLs). The techniques probed concern long-range electrostatic interactions, electrode charging (constant charge versus constant potential conditions), and electrolyte polarizability. Our simulations are performed on a quasi-two-dimensional, or slab-like, model capacitor, which is composed of a polarizable ionic liquid electrolyte, [EMIM][BF_4], interfaced between two graphite electrodes. To ensure an accurate representation of EDL differential capacitance, we derive new fluctuation formulas that resolve the differential capacitance as a function of electrode charge or electrode potential. The magnitude of differential capacitance shows sensitivity to different long-range electrostatic summation techniques, while the shape of differential capacitance is affected by charging technique and the polarizability of the electrolyte. For long-range summation techniques, errors in magnitude can be mitigated by employing two-dimensional or corrected three dimensional electrostatic summations, which lead to electric fields that conform to those of a classical electrostatic parallel plate capacitor. With respect to charging, the changes in shape are a result of ions in the Stern layer (*i.e.* ions at the electrode surface) having a higher electrostatic affinity to constant potential electrodes than to constant charge electrodes. For electrolyte polarizability, shape changes originate from induced dipoles that soften the interaction of Stern layer ions with the electrode. The softening is traced to ion correlations vertical to the electrode surface that induce dipoles that oppose double layer formation. In general, our analysis indicates an accuracy dependent differential capacitance profile that transitions from the characteristic camel shape with coarser representations to a more diffuse profile with finer representations.

I. INTRODUCTION

In response to a charged electrode, ionic liquids form electric double layers (EDLs). The EDL consists of alternating layers of cations and anions that screen the surface charge. Ionic liquid EDLs can have large values ($\sim$10-20 μF/cm^2) of differential capacitance, C_{dl}, which is the rate of change of surface charge density ($\langle\sigma\rangle$) with respect to surface potential ($\langle\Psi\rangle$) on a given electrode,

$$C_{dl} = \frac{\partial\langle\sigma\rangle}{\partial\langle\Psi\rangle}, \tag{1}$$

making them well suited for non-Faradaic energy storage. Recent experimental work has delineated the sensitive relationship of the C_{dl} of ionic liquids to atomic-level details of the EDL, including electrolyte molecular size[1] as well as electrode surface structure.[2–7] The key to improved energy storage lies in the optimization of these properties, which will require careful control of molecular level features. In this regard, theoretical techniques, especially those that capture the full atomic detail of the interface, will be a useful guide for future development.

Molecular dynamics (MD) has been broadly and successfully employed to understand both the structure of ionic liquids at electrified interfaces[8–17] as well as to estimate the electrode potential dependent differential capacitance.[18–28] A variety of ionic liquid interatomic potentials have been applied to the study of EDLs, including coarse grained,[19,29–31] all atom,[8–15,17,18,20–25,28,32,33] and polarizable models.[34–39] Coarse grain simulations of ionic liquids[19,29–31] have provided important insight into how ionic liquid size and shape influence the EDL structure and capacitance. For instance, coarse grained models[19,40] have been used extensively to corroborate mean field predictions that describe how disparities in ion size and packing at the electrode surface lead to the experimentally observed camel- and bell-shaped profiles of C_{dl} with respect to $\langle\Psi\rangle$. All atom interatomic potentials provide a richer representation of EDLs and have been used to detail both the electrode potential dependent structure and the differential capacitance of specific ionic liquid compounds.[8–15,17,18,20–25,28,32,33] The predictive power of these methods has been recently highlighted though the excellent agreement of MD derived EDL structures with atomic force microscopy measurements[41] and the ability to capture the magnitude and camel shaped profile of C_{dl}.[22–26,28] Adding a level of refinement beyond the all atom models, polarizable models of ionic liquids, where each atom has a dynamic dipole moment, have produced highly accurate measures of bulk structure and transport;[34–39] however, they have had limited application to the study of EDLs, with the only application at present being to organic electrolyte systems.[25]

Several methodologies have been developed for apply-

[a)] Electronic mail: justin.b.haskins@nasa.gov

ing charge or, alternatively, setting the potential of electrodes in a manner consistent with a metal in MD simulations. The most direct of these methods applies a constant charge to each electrode surface atom, referred to as constant-σ ensemble. Electrodes treated in this manner have produced favorable comparisons of C_{dl} with cyclic voltammetry measures on some carbon nanostructures.[18] A more complex approach is to redistribute the electrode surface charge over the course of the simulation such that the potential difference, $\Delta\Psi$, between two electrodes meets a pre-defined value. This approach, referred to as the constant-$\Delta\Psi$ ensemble,[42,43] has been employed to obtain the differential capacitance of ionic liquids at both ideal and roughened graphitic electrodes,[22–26,28] where the application of the constant-σ condition is not intuitive. Notably, the extensive simulations of Vatamanu and coworkers[23] using this approach have provided a detailed description of how the electrode surface, including spacing, curvature, and disorder, influences the magnitude and shape of C_{dl}.

In addition, numerical issues related to simulation methodology can affect the accuracy of EDL computations. Since slab-like, quasi-two-dimensional (2D) geometry is often employed in these computations (see Fig. 1), the appropriate technique for the long range electrostatic summation must be considered. Typically, such summations assume three dimensional (3D) periodicity, which conflicts with the quasi-2D symmetry of a slab in an infinite vacuum and introduces spurious electrostatic interactions between periodic images. To correct for this, the computationally costly, though exact, 2D Ewald summation[44] is often utilized. Alternatively, less expensive 2D corrections the the 3D Ewald summation have also been considered.[45] The comparative accuracy of these options, however, has yet to be rigorously determined.

Another source of potential error arises in the determination of C_{dl}, which is often computed as the numerical derivative of $\langle\sigma\rangle$ with respect to $\langle\Psi\rangle$ on a given electrode. Due to the slow dynamics of ionic liquids and the complexity of interfacial interactions, however, the noise present in the numerical derivative is often large. Reducing the noise requires fitting the $\langle\sigma\rangle$ data over many simulations using a fine voltage mesh and taking the derivative of the curve fit.[24] Alternatively, fluctuation formulas for C_{dl} have recently been derived,[30,31,46] which remove the ambiguity of a noisy numerical derivative and do not require many simulations over a dense potential grid. Thus, C_{dl} can be determined at particular points of interest. At present, the fluctuation formulas have not been extensively tested and are available for only two electrode systems treated with the constant-$\Delta\Psi$ approach. Furthermore, the available fluctuation expressions define the quantity $\partial\langle\sigma\rangle/\partial\Delta\Psi$, which is the total capacitance of two electrodes, a positive electrode and oppositely charged negative electrode, together as opposed to the capacitance of an individual electrode. Fluctuation expressions for the capacitance of individual electrodes, which are commonly measured in experiments, are necessary to describe differences in the EDL capacitance at negative and positive electrodes, leading, for example, to asymmetric, camel-shaped C_{dl} profiles.

Despite the considerable amount of work using MD simulations to study EDL structure and capacitance, issues related to simulation methodology have only begun to be examined recently.[29,47–49] In the present work, we evaluate the impact of different modeling approaches on the computed structure and capacitance of the EDL. We begin with an evaluation of the numerical accuracy of various long-range summation techniques on electrode potential and EDL structure. We then investigate the evaluation of differential capacitance using constant-σ and constant-$\Delta\Psi$ electrodes. For both electrode approaches, we derive, benchmark, and evaluate new fluctuation expressions for C_{dl} that extend previously derived expressions and enable the analysis of single electrodes. Differences in capacitance are then rationalized though an evaluation of the potential dependent density and the configuration of the surface ion layer, or Stern layer. Finally, we comment on the role of polarization on EDL structure and capacitance. To perform these simulations, we employ a model system consisting of an electrolyte, 1-ethyl-3-methylimidazolium boron tetrafluoride ([EMIM][BF_4]) as represented by the polarizable force field, APPLE&P,[50–52] interfaced between two ideal graphite electrodes (see Fig. 1).

II. METHODS

A. Long-Range Electrostatics

Our capacitor system has a slab-like, or quasi-2D, geometry, with the $\mathbf{r}_{\parallel}$ dimensions being fully periodic and the z dimension, normal to the surface, being finite. While the covalent interactions are local and easily amenable to such a geometry, the 3D periodic techniques typically employed to perform long-range summation of electrostatic interactions do not easily conform to slab-like geometry and can lead to spurious interactions between electrode images. There are various approaches that can be used to perform such a summation in slab geometry, which include the exact 2-D Ewald summation, the 3-D Ewald summation with a slab correction, and the 3-D Ewald summation with no correction.

The 2-D Ewald summation technique, as developed by Parry,[53] Heyes and coworkers,[54] and Leeuw and coworkers[55] and further streamlined by Kawata and Mikami,[44] is an exact method for the evaluation of the electrostatic interactions in a system having slab geometry. Similar to 3-D Ewald summation, one partitions the electrostatic energy as $U^{ES} = U^r + U^{k,2D}$, where U^r is the real space contribution and $U^{k,2D}$ is the reciprocal space contribution. The real space contribution is given by

$$U^r = \sum_i \sum_{j\neq i} \frac{q_i q_j}{|\mathbf{r}_{ij}|} \mathrm{erfc}(\alpha|\mathbf{r}_{ij}|), \tag{2}$$

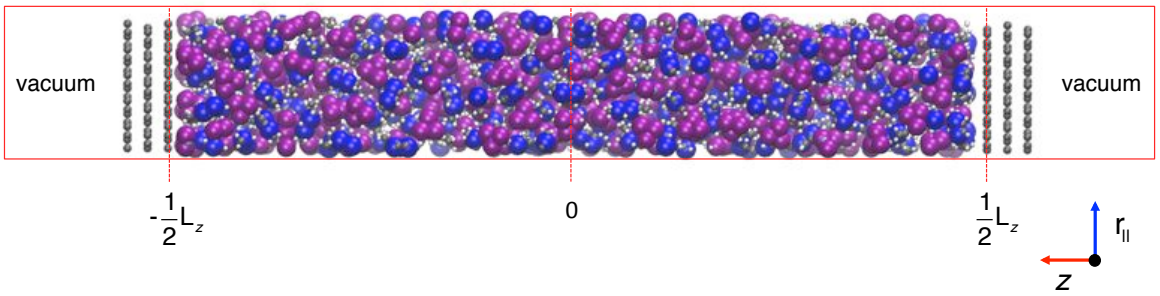

FIG. 1. Representation of dual graphite electrodes interfaced with [EMIM][BF_4]. The system has slab geometry and is periodic in the directions parallel to the electrode surface ($r_\parallel$) and non-periodic in the direction perpendicular to the electrode surface (z).Throughout this work, $z = 0$ is defined as the point equidistant to both electrodes. The spacing between the electrodes is defined as L_z, and beyond the electrodes an infinite vacuum is assumed. The large purple and blue atoms are F and N atoms, respectively, while the small grey and white atoms are C and H, respectively.

which represents the mutual interaction between atomic charges as well as the interaction of atomic charges with Gaussian distributed charges (the half maximum width of these distributions is $2\alpha^{-1}\sqrt{\ln(2)}$ Å which is standard to the Ewald procedure). Each Gaussian is centered on a given atom and bears opposite charge to that atom, screening the real space interaction and allowing the use of a cutoff. The long range interactions are handled through the reciprocal space summation over a grid of k-point in the $\mathbf{r}_\parallel$ directions according to

$$U^{k,2D}_{\mathbf{k}_\parallel\neq 0} = \frac{1}{\mathbf{A}_\parallel}\sum_{\mathbf{k}\neq 0}\int_{-\infty}^{\infty} \mathrm{d}h \frac{1}{|\mathbf{k}_\parallel|^2+h^2}\times \exp\left(-\frac{|\mathbf{k}_\parallel|^2+h^2}{4\alpha^2}\right)|S_{2D}(\mathbf{k}_\parallel,h)|^2, \tag{3}$$

where $A_\parallel$ is the area of the simulation cell in the $\mathbf{r}_\parallel$ directions, $\mathbf{k}_\parallel$ are reciprocal space points the $\mathbf{r}_\parallel$ directions, h is a real space integration variable in the direction of z, and $S_{2D}(\mathbf{k}_\parallel,h) = \sum_{j=1}^{N} q_j \exp(i\mathbf{k}_\parallel\cdot\mathbf{r}_{\parallel,j} + ihz_j)$. Unlike the 3-D Ewald summation, the infinite contribution at $\mathbf{k}_\parallel = 0$ is dependent on the z direction according to

$$U^{k,2D}_{\mathbf{k}^\parallel=0} = -\frac{1}{A^\parallel}\sum_{i=1}^{N}\sum_{j=1}^{N} q_i q_j \times \left\{\frac{\sqrt{\pi}}{\alpha}\exp(-[\alpha z_{ij}]^2) + \pi z_{ij}\mathrm{erf}(\alpha z_{ij})\right\}. \tag{4}$$

Such an N^2 contribution is not easily computed for large systems without the use of basis splines, which reduce this term to an order N operation. In the present work, we compute this term exactly at 100 values of z and employ 4^{th} order basis splines to evaluate this quantity at all atomic positions.

Alternatively, the relatively less computationally expensive 3-D Ewald summation with an approximate correction for slab-like geometry can be employed. In this approach, a large amount of vacuum space is included between the capacitor periodic images in the z direction such that the electrostatic interactions between the images is considered small. The correction to the 3D-Ewald summation, as given by Yeh and coworkers,[45] may be implemented to remove the remaining long-range interaction between the electrode images in the z direction. Though originally developed for systems of interacting point charges, we have extended this correction to account for the long-range interaction of point charges with the atomic dipoles produced from the polarizable force field according to

$$U^{2D}_{corr} = \frac{1}{2\epsilon_0}M_z^2, \tag{5}$$

where ϵ_0 is the permittivity of free space and M_z is the net dipole moment in the z direction, $\sum_{i=1}^{N}(q_i z_i + \mu_z)$. We use a vacuum three times larger than the electrode separation.

B. Constant Potential versus Constant Charge Electrodes

In the present work, our model capacitor consists of electrodes composed of three layers of graphite, as shown in Fig. 1. The position of an atom, $\mathbf{r}$, is decomposed into the direction normal to the electrode surface, z, and the directions parallel to the electrode surface, $\mathbf{r}_\parallel$. The electrodes are separated by a distance L_z, and the region beyond the electrodes in the z direction is considered infinite vacuum. To characterize the double layers at each surface accurately, it is important that they do not interact. Accordingly, we find $L_z = 10$ nm meets this criteria; however, for computational ease, select benchmarking simulations are performed with smaller $L_z = 4$ nm systems. The electrode atoms interact with the ionic liquids through both repulsive-dispersive Lennard-Jones interactions as well as electrostatic interactions,

though the atomic positions are held fixed throughout the dynamics. To approximate a metallic surface, the charges on the electrode atoms are taken to be Gaussian distributed with a width at half maximum of $\sqrt{\ln(2)}$ Å.

Two approaches are employed in the present work to induce a potential on the electrodes: the constant-$\Delta\Psi$ emsemble and the constant-σ ensemble. For the constant-$\Delta\Psi$ ensemble, the charges on the electrodes are determined through a modified version of the constant potential formalism first implemented by Siepmann[42,43] that ensures all atoms on a given electrode are at an identical electrostatic potential and that the potential difference between the two electrodes is at the defined target value, $\Delta\Psi$. Similar approaches have found use in simulations of ionic liquids in the presence of electrified interfaces.[24,27,48] In this method the system Hamiltonian, H, for our dual electrode, model capacitor is given by

$$H = U^K + U^{RD} + U^{ES} - A|\sigma|\Delta\Psi, \tag{6}$$

where U^K is the kinetic energy, U^{RD} is the total repulsive-dispersive energy, U^{ES} is the total electrostatic energy, A is the electrode cross sectional area, $|\sigma|$ is the absolute value of the electrode surface charge density on the positive (σ^+) or negative (σ^-) electrode, and $\Delta\Psi$ is the imposed potential difference between positive and negative electrodes, given by $\Psi^+ - \Psi^-$. This Hamiltonian results from a constrained optimization that distributes charges on the electrode atoms such that $\sigma^+ = -\sigma^-$. Thus, all atoms on a given electrode are at an identical electrostatic potential, and the potential difference between the electrodes is the defined value of $\Delta\Psi$. For clarity, throughout the majority of this work the superscripts + and − are not explicitly given, but are indicated through the sign of the surface potential or the charge.

An alternative to treating the electrodes in the constant-$\Delta\Psi$ ensemble is to simply define a static charge distribution on the electrode, referred to as the constant-σ ensemble. For our model capacitor, we distribute equal charge to all surface atoms (*i.e.* those on the graphite plane nearest the liquid) on a given electrode and ensure $\sigma^+ = -\sigma^-$. The Hamiltonian in this case is simply, $H = U^K + U^{RD} + U^{ES}$. Care must be taken when defining the electrode potential, however, as

$$\Psi = \frac{\partial H}{\partial \sigma} = \frac{1}{N}\sum_i \frac{\partial H}{\partial q_i}\frac{\partial q_i}{\partial \sigma}, \tag{7}$$

which implies any electrode atom, "i," not participating in the charging process ($\partial q_i/\partial\sigma = 0$) should not be included in the potential computation. For the present work, because we smear charge only on the graphite plane nearest the electrolyte, we tabulate the potential on only atoms in this plane. This method is clearly more straightforward than the constant-$\Delta\Psi$ formalism; however, as the surface structure grows in complexity, the assignment of charges in this manner may not be trivial.

C. Capacitance Fluctuation Formulas

For the constant-$\Delta\Psi$ ensemble, the Helmholtz free energy of our model capacitor can be written as $F = -\beta^{-1}\ln(\Omega)$, where β is the inverse product of Boltzmann's constant and temperature and Ω the partition function of our system. The partition function is equal to $\int e^{-\beta H} dRdP$, where $\int ...dRdP$ represents a phase space integration and H is given by Eq. 6. The derivative of F with respect to $\Delta\Psi$ may then be written as,

$$\frac{\partial F}{\partial \Delta\Psi} = -A\langle|\sigma|\rangle - A\Delta\Psi\left\langle\frac{\partial|\sigma|}{\partial\Delta\Psi}\right\rangle + \left\langle\frac{\partial U^{ES}}{\partial\Delta\Psi}\right\rangle, \tag{8}$$

where $\langle ...\rangle$ represents the ensemble average of a given quantity. The final two terms that describe the ensemble average of the derivatives of $|\sigma|$ and U^{ES} with respect to $\Delta\Psi$ arise from the implicit, and instantaneous, dependence of the electrode charge on $\Delta\Psi$ introduced through our constant-$\Delta\Psi$ formalism. The integral of Eq. 8 with respect to $\Delta\Psi$ gives a direct means to obtain differences in free energy from molecular dynamics simulations. We include this expression here to provide a complete outline of the thermodynamics of our model capacitor system. Further evaluation and implementation of this expression can be found in an alternate work.[56]

Expressions for the differential capacitance of our model system can also be derived.[31,46,57,58] The average surface charge of our constant-$\Delta\Psi$ electrode is given by $\langle\sigma\rangle = \Omega^{-1}\int \sigma e^{-\beta H} dRdP$. As described in recent work,[31,46] the derivative of $\langle\sigma\rangle$ with respect to $\Delta\Psi$ yields the combined differential capacitance of the two electrodes in our model capacitor. This quantity can be written as

$$\begin{aligned}\frac{\partial\langle\sigma\rangle}{\partial\Delta\Psi} =& \beta A\left\langle|\sigma|\delta\sigma\right\rangle + \left\langle\frac{\partial\sigma}{\partial\Delta\Psi}\right\rangle \\ &+ \beta A\Delta\Psi\left\langle\frac{\partial|\sigma|}{\partial\Delta\Psi}\delta\sigma\right\rangle - \beta\left\langle\frac{\partial U^{ES}}{\partial\Delta\Psi}\delta\sigma\right\rangle,\end{aligned} \tag{9}$$

where β is the inverse product of Boltzmann's constant and temperature, U^{ES} is the electrostatic energy, and $\delta\sigma = \sigma - \langle\sigma\rangle$. Eq. 9 is the full fluctuation formula for the total differential capacitance of two electrodes in the constant-$\Delta\Psi$ ensemble. The final three terms in Eq. 9, which have not been included in previous derivations of $\partial\langle\sigma\rangle/\partial\Delta\Psi$, account for the implicit dependence of electrode charge on the value of $\Delta\Psi$. For the system studied here, the first term on the right side of Eq. 9 is by and large the leading contribution to the total differential capacitance. Included in the second and third terms, $\langle\partial\sigma/\partial\Delta\Psi\rangle$ represents the self-capacitance of the electrodes under the influence of the electrolyte structure. Similarly, in the fourth term, $\langle\partial U^{ES}/\partial\Delta\Psi\rangle$ is dominated by changes in the self-energy of the electrode. The value of $\langle\partial\sigma/\partial\Delta\Psi\rangle$, being the capacitance of the electrode only, is an order of magnitude smaller than $\beta A\langle|\sigma|\delta\sigma\rangle$, though non-negligible. We find that $\langle\partial\sigma/\partial\Delta\Psi\rangle$ and $\langle U^{ES}/$

$\partial\Delta\Psi\rangle$ are relatively constant for the model system considered in the present work. As such, the final two terms in Eq. 9 that include fluctuations of these values are vanishingly small. We thereby truncate the expression after the first two terms. For other systems, however, these terms may not be negligible.

Of experimental interest, the resolution of capacitance for a single electrode, $\partial\langle\sigma\rangle/\partial\langle\Psi\rangle$, yields information on the comparative behavior of the EDL at positive and negative potential conditions. An expression for $\partial\langle\sigma\rangle/\partial\langle\Psi\rangle$, which has not previously been reported, can be derived for use with our model capacitor system by starting with an expansion of differential capacitance,

$$\frac{\partial\langle\sigma\rangle}{\partial\langle\Psi\rangle} = \frac{\partial\langle\sigma\rangle}{\partial\Delta\Psi}\frac{\partial\Delta\Psi}{\partial\langle\Psi\rangle}, \tag{10}$$

where the ensemble averages, $\langle\sigma\rangle$ and $\langle\Psi\rangle$, are taken to be on the same electrode. The average potential on one of our electrodes is given by $\langle\Psi\rangle = \Omega^{-1}\int \Psi e^{-\beta H} dRdP$. As with surface charge previously, the derivative of this quantity with respect to $\Delta\Psi$ may be taken to yield

$$\begin{aligned}\left[\frac{\partial\Delta\Psi}{\partial\langle\Psi\rangle}\right]^{-1} &= \beta A\left\langle|\sigma|\delta\Psi\right\rangle + \left\langle\frac{\partial\Psi}{\partial\Delta\Psi}\right\rangle \\ &+ \beta A\Delta\Psi\left\langle\frac{\partial|\sigma|}{\partial\Delta\Psi}\delta\Psi\right\rangle - \beta\left\langle\frac{\partial U}{\partial\Delta\Psi}\delta\Psi\right\rangle,\end{aligned} \tag{11}$$

where $\delta\Psi = \Psi - \langle\Psi\rangle$. For the systems of interest in the present work, we have found, numerically, that $\left\langle\frac{\partial\Psi}{\partial\Delta\Psi}\right\rangle$, representing the instantaneous change of electrode potential with a change in potential difference, is 0.5 and -0.5 for the positive and negative electrodes, respectively, to within the nearest thousandth. For reasons previously described, the final two terms in Eq. 11 are vanishingly small and are not included in the current computations. The total expression for differential capacitance for either the positive or negative electrodes is then given as

$$\begin{aligned}\mathrm{C}_{\Delta\Psi} = \frac{\partial\langle\sigma\rangle}{\partial\langle\Psi\rangle} &= \left[\beta A\left\langle|\sigma|\delta\sigma\right\rangle + \left\langle\frac{\partial\sigma}{\partial\Delta\Psi}\right\rangle\right]\times \\ &\left[\beta A\left\langle|\sigma|\delta\Psi\right\rangle + \left\langle\frac{\partial\Psi}{\partial\Delta\Psi}\right\rangle\right]^{-1},\end{aligned} \tag{12}$$

where $C_{\Delta\Psi}$ indicates capacitance in the constant-$\Delta\Psi$ ensemble.

Complementary thermodynamic expressions can be derived for our model capacitor in the constant-σ ensemble. The Helmholtz free energy can again be determined from $F = -\beta^{-1}\ln(\Omega)$; however, the simpler form of the constant-σ Hamiltonian when compared to that of the constant-$\Delta\Psi$ case leads to

$$\frac{\partial F}{\partial\sigma} = \sum_i \frac{\partial F}{\partial q_i}\frac{\partial q_i}{\partial\sigma}. \tag{13}$$

As a constant value is used for each surface charge atom, $\partial F\partial\sigma$ further reduces to $\langle\Psi\rangle$, the average potential on the electrode. Concerning capacitance using constant-σ electrodes, the quantities of interest are $\partial\sigma/\partial\langle\Delta\Psi\rangle$ and $\partial\sigma/\partial\langle\Psi\rangle$, where the potential difference between the electrode and the potential of each electrode are ensemble averages as the potential is free to fluctuate in time. Employing a procedure similar to that used for the constant-$\Delta\Psi$ ensemble, the fluctuation expressions can be written as

$$\frac{\partial|\sigma|}{\partial\langle\Delta\Psi\rangle} = \left[\left\langle\frac{\partial\Delta\Psi}{\partial|\sigma|}\right\rangle - \beta A\left\langle\Delta\Psi\delta\Delta\Psi\right\rangle\right]^{-1} \tag{14}$$

and

$$\mathrm{C}_\sigma = \frac{\partial\sigma}{\partial\langle\Psi\rangle} = \left[\left\langle\frac{\partial\Psi}{\partial\sigma}\right\rangle - \beta A\left\langle|\Psi|\delta\Delta\Psi\right\rangle\right]^{-1}, \tag{15}$$

where $\delta\Delta\Psi = \Delta\Psi - \langle\Delta\Psi\rangle$ and C_σ indicates capacitance in the constant-σ ensemble.

D. Polarizable Force Field

We employ the atomistic polarizable potential for liquids, electrolytes, and polymers (APPLE&P)[50–52] to represent [EMIM][BF_4]. In this potential, each atom has a polarizability, α, which induces an atomic dipole, $\boldsymbol{\mu}$, according to

$$\boldsymbol{\mu}_i = \alpha_i \cdot \mathbf{E}_i, \tag{16}$$

where $\mathbf{E}_i$ is the electric field due to charge-charge and charge-dipole interactions at atomic site i. The dipoles are iteratively evaluated at each step of the simulation until the polarization energy converges to within 1E-9 kcal/mol. The polarization energy, U^{pol}, can be given as

$$U^{pol} = -\frac{1}{2}\sum_i \boldsymbol{\mu}\cdot\mathbf{E}_i^0, \tag{17}$$

where $\mathbf{E}_i^0$ is the charge contribution to the electric field. Because the dipole-charge interactions are long range, we have extended both the 2D and 3D Ewald summations to include contributions from charge-dipole interactions. The dipole-dipole interactions are alternatively treated with a reaction field to approximate their long-range interactions during the iterative update procedure. For all long-range techniques, the **k**-space grid is chosen to produce a 0.01% error in the long-range energy.

E. Molecular Dynamics Simulations

All simulations are performed in the canonical ensemble using the Nosé-Hoover formalism having a temperature of 363 K. The rRESPA formalism is used for time integrate, with the time step being 3 fs. We employ three rRESPA levels, with bonds, angles, and dihedrals being determined on the first level; impropers and nonbonded interactions between atoms no further than 6 Å

apart being determined on the second level; and all nonbonded interactions, long-range interactions, dipole updates, and surface charge updates being performed on the third level. There are 9 first level integrations and 3 second level integrations for every 3 fs outer integration. For the constant-$\Delta\Psi$ simulations, the potential is updated in the 3^{rd} rRESPA step, and the charges are determined such that the variance of Ψ on each atom is within 0.025 V of the electrode average. As previously mentioned, our model capacitor is composed of two electrodes, a positive and negative electrode, between which is the ionic liquid electrolyte. The electrodes are composed of three layers of graphite having the basal plane exposed to the electrolyte. For our investigation into the influence of method on EDL structure and capacitance, we use a *large* capacitor system with $L_z = 10$ nm and 216 [EMIM][BF_4] pairs, which, based on average ion density profiles, is free of size errors related to the interaction of the EDLs of the positive and negative electrodes. In a limited number of numerical tests, however, we also employ a *small* capacitor with an electrode spacing, $L_z = 4$ nm and 140 [EMIM][BF_4] pairs as an efficient means of comparing the accuracy of various methods.

III. RESULTS

A. Long-Range Electrostatics

To begin our study on differential capacitance, we address the issue of the performance of electrostatic summation techniques with respect to accuracy of the electrode potential and EDL structure. To do this, we use a small capacitor system consisting of [EMIM][BF_4] interfaced with electrodes $L_z = 4$ nm apart at 363 K, which allows the efficient comparison of our most expensive, and accurate, numerical methods to those having approximations that reduce computational expense.

Ideally, our model capacitor should electrostatically conform to the slab condition, periodic in the plane of the electrode and having infinite vacuum exterior to the electrode. To understand the implications of this condition on the electrostatic potential, we refer to the classical case of parallel plate capacitors separated by a distance L_z and having uniform charge densities of $\pm\sigma$. For such a system, the magnitude of the electric field between the plates is σ/ϵ_0, while the field is zero external to the plates. The lack of electric field external to the plates indicates that the potential is constant in these regions, and a path integral yields a potential difference of $\sigma L_z/\epsilon_0$ between the plates. A direct extension of this model to that of a parallel plate capacitor filled with a medium of a given dielectric constant yields similar results. Therefore, for our model capacitor to be consistent with the classical electrostatic system, the potential external to the electrodes should be constant. Some deviation from this behavior, however, could be expected near the electrodes because the charges in our system are localized to atoms.

To compare the behavior of the multiple electrostatic summation techniques in this respect, we provide a measure of the electrostatic potential averaged in the $r_{\|}$ directions, given as a function of z in Fig. 2 for our small capacitor in the constant-$\Delta\Psi$ ensemble. We immediately note a distinct difference between the 3D-Ewald and the other summation techniques. This is, in part, because the 3D Ewald summation necessitates the use of a periodic boundary condition in the z direction, which has been applied to allow a vacuum of $3L_z$ to separate the electrode periodic images, leading to a periodic boundary at ± 80 Å. Because of periodicity in the perpendicular direction in the 3D-Ewald approach, the potential must necessarily cross zero in the vacuum region, which is seen at the intersection of the potential from the positive and negative electrodes at the periodic boundary. According to our assumption of an infinite medium beyond the boundary of the electrodes, the 2D-Ewald and 3D/slab Ewald techniques conform with our expectations from the parallel plate capacitor model, having constant potential for $|z| > \frac{1}{2}L_z$. Interestingly, the internal structure of the ionic liquid appears similar between the three summation techniques.

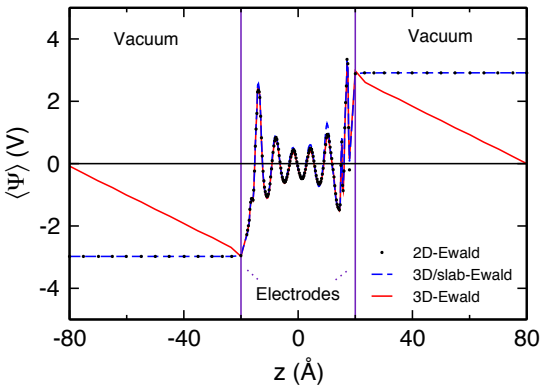

FIG. 2. Electrostatic potential profiles obtained from an $L_z = 4$ nm capacitor having a constant $\Delta\Psi$ of 6 V. The profiles are obtained from simulations employing the 3D-Ewald (dashed line), the 2D-Ewald (dotted line), and the 3D/slab-Ewald (solid line) summation techniques. The profiles are shown from the center of the capacitor to $z = 80$ Å, which represents the periodic boundary for the 3D and 3D/slab-Ewald techniques.

To better understand the implications of the various potential profiles, we examine the relationship between σ and $\Delta\Psi$ using the different electrostatic summation techniques for our model capacitor systems in the constant-$\Delta\Psi$ and constant-σ ensembles, given in Fig. 3. In both electrode ensembles, we find the 3D/slab-Ewald approach to be commensurate with the 2D-Ewald correction. Between the constant-$\Delta\Psi$ and constant-σ values using these summation techniques, we see close agreement, which suggests the average σ-$\Delta\Psi$ relationship is weakly dependent on electrode conditions for the ideal graphite system

used here. For the 3D-Ewald summation, we find different behaviors that depend on the specific electrode conditions. For constant-$\Delta\Psi$ electrodes, shown in Fig. 3a, we find that average surface charge, $\langle\sigma\rangle$, is overestimated by 5-10%, which is a result of the interaction between oppositely charged electrodes across the vacuum. The reduced potential is compensated by a larger $\langle\sigma\rangle$. For constant-σ electrodes, shown in Fig. 3b, the average potential drop, $\langle\Delta\Psi\rangle$, is an underestimate of the 3D/slab and 2D Ewald techniques, again due to interaction across the vacuum. Across the range of explored values, the overestimation of $\langle\sigma\rangle$ and the underestimation of $\langle\Delta\Psi\rangle$ for constant-$\Delta\Psi$ and σ electrodes, respectively, by the 3D-Ewald summation is ∼5-10%. The error in the estimates of $\langle\sigma\rangle$ and $\langle\Delta\Psi\rangle$ using the 3D-Ewald approach directly translates to a 10-20% error in differential capacitance of a single electrode, which is approximately twice the derivate of surface charge with respect to the potential difference between the two electrodes.

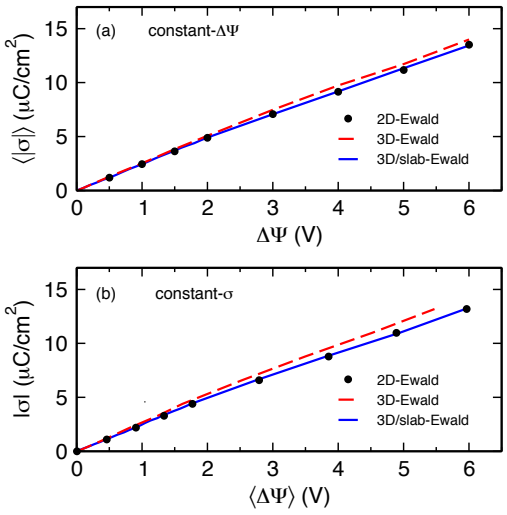

FIG. 3. Influence of long-range electrostatic summation (2D, 3D, and 3D/slab Ewald summation) on the σ-Ψ relationship of the $L_z = 4$ nm model capacitor for both (a) constant-$\Delta\Psi$ and (b) constant-σ conditions.

While the potential on the electrode is affected by the choice of long range summation technique, the associated influence on structure is not clear. To probe structural effects, we have computed the ion density profile (ρ) along z using the three summation techniques as well as the deviation of ρ obtained by the 3D Ewald and 3D/slab Ewald from that of the 2D-Ewald technique ($\delta\rho$) for the constant-$\Delta\Psi$ and σ conditions. The density profiles, as shown in Fig. S1a and b of the supplemental material,[59] indicate that all three summation techniques for both electrode conditions result in almost identical measures of ρ. An analysis of the $\delta\rho$, given in Fig. S1c and d,[59] indicates that the resulting deviation in density when using 3D/slab-Ewald and 3D-Ewald summations is only a few percent. The similarity in the magnitude of $\delta\rho$ between the two techniques indicates the structure is relatively insensitive to the up to 10% error in σ or $\Delta\Psi$ inherent to the 3D-Ewald summation.

Our results suggests that the 3D/slab-Ewald summation technique is appropriate for the system of interest here, providing an accuracy comparable to the 2D-Ewald summation with the lower computational expense of the 3D-Ewald summation technique. For other more general systems, we conjecture that the 3D/slab-Ewald will be a good approximation to the exact 2D-Ewald approach if the periodic slab images are sufficiently separated such that their leading interaction is dipolar in nature. In the remainder of this work, therefore, we apply the 3D/slab-Ewald summation technique. With regards to the constant-$\Delta\Psi$ and constant-σ ensembles, our results suggest both methods behave in a qualitatively similar manner. As shown in Fig. 3, the σ-$\Delta\Psi$ relationship is similar for both surface conditions, leading to our expectation of similar magnitudes of differential capacitance.

B. Electrode Ensemble: Capacitance Sensitivity

We now turn to an investigation of the comparative behavior of differential capacitance in the constant-$\Delta\Psi$ and constant-σ ensembles. We first describe the general behavior and function of the terms present in the fluctuation expressions used to compute C_{dl}. For the expression for constant-$\Delta\Psi$ electrodes in Eq. 12, the dominant terms include $\beta A\langle|\sigma|\delta\sigma\rangle$, $\langle\partial\sigma/\partial\Delta\Psi\rangle$, and $\beta A\langle|\sigma|\delta\Psi\rangle$. The value of $\beta A\langle|\sigma|\delta\sigma\rangle$ and $\langle\partial\sigma/\partial\Delta\Psi\rangle$ on the positive and negative electrodes are of equal magnitude but opposite sign as $\sigma^+ = -\sigma^-$. Alternatively, the value of $\beta A\langle|\sigma|\delta\Psi\rangle$ is of equal magnitude and sign for both electrodes because $\Delta\Psi = \Psi^+ - \Psi^-$ is constant. The function of $\beta A\langle|\sigma|\delta\sigma\rangle$ is to include the capacitance that is primarily attributed to electrolyte interaction with the electrode, while $\langle\partial\sigma/\partial\Delta\Psi\rangle$ encapsulates the self-capacitance of the electrodes. Any asymmetry in $C_{\Delta\Psi}$ related to the different screening properties of the EDL at the positive and negative electrodes is manifested through $\beta A\langle|\sigma|\delta\Psi\rangle$. From Eq. 12, we then see that from a single simulation at a given value of $\Delta\Psi$, two values of $C_{\Delta\Psi}$ are obtained using $\frac{\partial\langle|\sigma|\rangle/\partial\Delta\Psi}{\langle\partial\sigma/\partial\Delta\Psi\rangle\pm\beta A\langle|\sigma|\delta\Psi\rangle}$, where the addition or subtraction in the denominator yields the capacitance of the positive and negative electrode, respectively. With regard to the simpler fluctuation expression used for constant-σ electrodes, Eq. 15, both $\langle\partial\Psi/\partial\sigma\rangle$ and $\beta A\langle\Delta\Psi\delta|\Psi|\rangle$ are positive for both electrodes. As with the constant-$\Delta\Psi$ expression, the capacitance contribution from the liquid and self-capacitance of the electrode are primarily contained in the $\langle\partial\Psi/\partial\sigma\rangle$ and $\beta A\langle\Delta\Psi\delta|\Psi|\rangle$ terms, respectively.

We now perform a convergence study on $\partial\langle\sigma\rangle/\partial\langle\Psi\rangle$, as defined in Eq. 12, on our prototype $L_z = 4$ nm capacitor using the constant-$\Delta\Psi$ ensemble for potential differences

of 0, 2, and 4 V. Regarding the value of $\beta A\langle|\sigma|\delta\sigma\rangle$, shown in Fig. 4a, we find the magnitude reaches to within 10% of its long-time average after ∼10 ns. Longer simulations lead to subtle variations, which can be seen in the crossing of the value of $\beta A\langle|\sigma|\delta\sigma\rangle$ for 0 and 2 V potential differences near 45 ns. These long time processes that affect capacitance are difficult to characterize and are likely related to minor changes in the EDL structure, such as the ion density at the electrode surface. We have also provided a measure of the instantaneous derivative of surface charge with respect to surface potential, $\langle\partial\sigma/\partial\Psi\rangle$, as a function of simulation time. As given in Fig. 4b, this term converges within ∼ 10 ns and is nearly constant and for multiple values of $\Delta\Psi$, exhibiting variations on the order of 10^{-3}, which are orders of magnitude smaller than the total value of capacitance. We therefore conclude that this term is effectively constant across our potential difference range and here further determine its value from a single simulation at $\Delta\Psi = 0$ V. The third term, $\beta A\langle|\sigma|\delta\Psi\rangle$, in Fig. 4c also shows similar convergence trends with the prior two terms. It is important to note that at $\Delta\Psi = 0$ V, this term is nearly zero, which is necessary as the positive and negative electrodes are identical in this case. Furthermore, the value of this term at 2 and 4 V is small, and this indicates that in our specific system, there is little difference between the capacitance of the positive and negative electrodes.

The convergence behavior of $\partial\sigma/\partial\langle\Psi\rangle$ for constant-σ electrodes is qualitatively similar to that of the constant-$\Delta\Psi$ electrodes. The value of $\beta\mathrm{A}\langle|\Psi|\delta\Delta\Psi\rangle$, shown in Fig. 4d, shows reasonable convergence within ∼25 ns, which is longer than required for constant-$\Delta\Psi$ electrodes. The value of fluctuations on constant-σ electrodes may converge more slowly due to harder electrostatic interactions between the electrode and surface ions when compared to the constant-$\Delta\Psi$ electrodes, where the charge redistributes on the electrode in response to the surface ion environment and could lead to a more favorable ion interactions. As given in Fig. 4e, the value of $\langle\partial\Psi/\partial\sigma\rangle$ appears to be converged again within 25 ns, though the spread in values is relatively small, on the order of 10^{-3}. Based on our convergence tests, all further measures of differential capacitance in the present work are obtained from 50-100 ns simulations.

To better understand the effect of electrode ensemble, we compare the differential capacitance of our prototype $L_z = 4$ nm system using constant-$\Delta\Psi$ and σ electrodes as obtained from both fluctuation expressions and numerical derivatives of σ with respect to Ψ. To provide a σ profile sufficiently dense enough in Ψ space to take a numerical derivative, we have performed 11 simulations equally spaced between 0 and 2 V for the constant-$\Delta\Psi$ condition and between 0 and 4.44 μC/cm^2 for the constant-σ condition. Beyond these limits, we have performed additional simulations at 3 V (6.58 μC/cm^2) and 4 V (8.78 μC/cm^2) for the constant-$\Delta\Psi(\sigma)$ electrodes. Following previous approaches,[27] σ is fit to a high order polynomial, the derivative of which provides a smooth, well-behaved measure of C_{dl}. Furthermore, we fit the results of our fluctuation formulas to a high order polynomial to highlight the general trends in differential capacitance. The exact values resulting from the fluctuation formula as well as the derivative of surface charge as obtained from a central differences approach of raw data are shown in Fig. S2 of the supplemental material.[59] The result of this procedure, shown in Fig. 5, indicates that the fluctuation expressions provide close agreement with the numerical derivative approach. This validates our fluctuation expressions for different electrode ensembles and enables the treatment of larger systems, where obtaining a dense $\sigma(\Psi)$ curve is prohibitively expensive.

While there are minor variances between capacitances obtained with different electrode conditions, both the magnitude and global, camel-shaped profile of C_{dl} are similar. However, the prototype system used to obtain these results necessarily introduces confinement effects into the measure of C_{dl}. We therefore perform computations on larger $L_z = 10$ nm systems to remove size effects, the results of which are shown in Fig. 6. Following our previous convention, we show a fit to the fluctuation formula results to highlight trends in the data, while the exact values can be found in Fig. S3 of the supplemental material.[59] As with the smaller capacitor, the magnitude of differential capacitance is similar between the constant-$\Delta\Psi$ and constant-σ ensembles, each resulting in averaged capacitances of 4.8 $\mu F/cm^2$. We also note that for both electrode ensembles the value of capacitance is larger at negative potentials that at positive potentials. A few differences, however, are apparent between the ensembles. Constant-σ electrodes produce a highly resolved camel-shaped profile (akin to expectations from mean field theory), with the peaks being centered on ±0.5 V, while constant-$\Delta\Psi$ electrodes lead to a more diffuse capacitance with lower maximum values. The value of surface potential at $\Delta\Psi = 0$ and $\sigma = 0$, or the potential of zero charge, is virtually zero for our system in both electrode ensembles, which somewhat appears to be nearer to the maximum in $C_{\Delta\Psi}$ at negative potentils on constant-$\Delta\Psi$ electrodes and in a well between the dual peaks of the camel-shaped C_σ on constant-σ electrodes. At larger magnitudes of potential ($> |1|$ V), constant-$\Delta\Psi$ electrodes have larger values of differential than constant-σ electrodes. The error associated with both measures of capacitance, shown in Fig. S3, are obtained from the standard deviation of C_{dl} as a function of simulation length and are similar in magnitude for both electrode systems, ∼0.1-0.2 μF/cm^2.

C. Electrode Ensemble: Structural Sensitivity

To understand the origin of the noted differences in C_{dl} with respect to electrode ensemble, we now investigate the potential dependent structural behavior of the EDL from the $L_z = 10$ nm capacitor. As a first step in this direction, we have evaluated the ion density (ρ) as

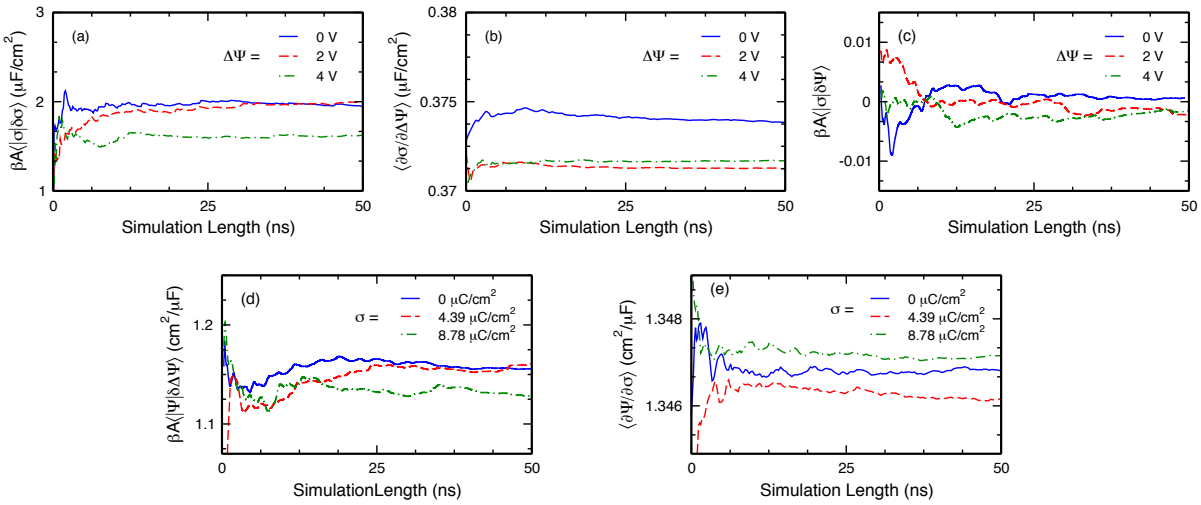

FIG. 4. Convergence of terms in Eqs. 12 and 15, which is used to compute C_{dl} with constant-$\Delta\Psi$ and constant-σ electrodes, respectively, as a function of total simulation time. Results are obtained from an $L_z = 4$ nm model capacitor and are shown for constant $\Delta\Psi$ values of 0, 2, and 4 V and for constant σ values that produce similar values of potential difference, 0, 4.39, and 8.78 μC/cm^2.

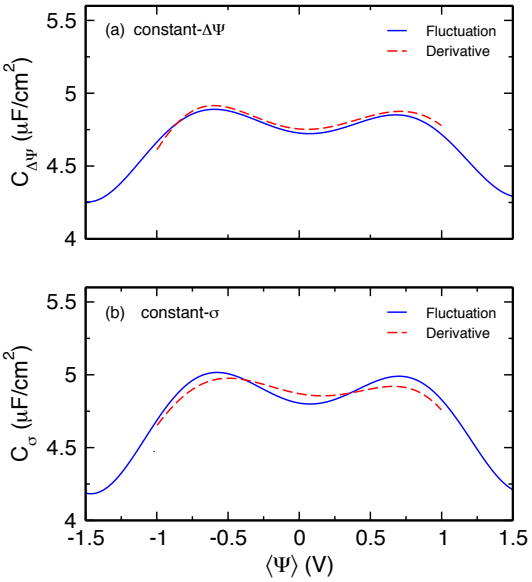

FIG. 5. Comparison of the differential capacitance obtained from $L_z = 4$ nm systems having (a) constant-$\Delta\Psi$ and (b) constant-σ electrodes. Capacitance from both the fluctuation formulas (solid lines) as well as the numerical derivative of the charge density (dashed lines) are provided.

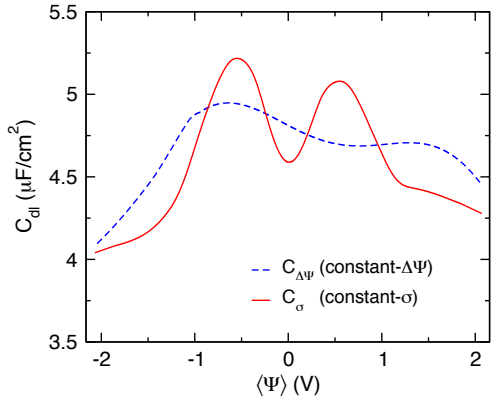

FIG. 6. Differential capacitance of an $L_z = 10$ nm capacitor as obtained from the use of constant-$\Delta\Psi$ (dashed lines) and constant-σ (solid lines) electrodes.

a function of distance (Δz) from both constant-$\Delta\Psi$ and constant-σ electrodes, shown for neutral, negative, and positive electrodes in Fig. S4 of the supplemental material. For the case of neutral electrodes displayed in Fig. 4a and b, the total density, which includes both cations and anions, shows a sharp signature within $\Delta z < 5$ Å, indicating a dense layer of adsorbed ions at the electrode surface. The electrode surface ion layer shares similarities with the Stern layer, which in the classical picture of the EDL is the layer closest to the surface. Less prominent accumulations in ρ occur at larger values of Δz, $5 < \Delta z < 15$ Å, and represent the liquid response to the ordering and possible imbalance of cations and anions in the surface ion layer. Further decomposing ρ into its ionic components, the surface ion layer shows a single, strong cation signature near the surface and two primary anion signatures, one overlapping the cation signature and one more distance from the surface. This

suggests a finer structure within the surface ion layer, where anions assume district configurations. Comparing ρ between the two electrode conditions, the surface ion layer at the constant-$\Delta\Psi$ electrodes (Fig. S4a) has a higher initial peak than the one at the constant-$\Delta\sigma$ electrodes (Fig. S4b). This implies constant-$\Delta\Psi$ electrodes lead to a denser surface ion layer. Such a result is plausible considering the electrode charges respond to the surface ion environment in the constant-$\Delta\Psi$ approach, allowing for more energetically favorable charge distributions than that of the constant-σ approach and thus stronger ion binding at the surface.

Extending our analysis of the EDL density, we provide ρ profiles for electrodes having a constant $\Delta\Psi$ of 4.2 V or, equivalent in terms of potential, a constant-$|\sigma|$ of 9.63 μC/cm^2. The density as a function of Δz from the positive electrodes is shown in Fig. S4c and d, while density from the negative electrodes is shown in Fig. S4e and f. Beyond the expected differences of a cation and anion dominated surface ion layer at the negative and positive electrodes, respectively, the same general structure described for the neutral electrode is present at the charged surfaces. This includes a strong signature at small Δz, representing the surface ion layer, and less prominent signatures at larger Δz, representing ion accumulations that compensate for an imbalance of cations and anions in surface ion layer. The surface ion layer occurs at $\Delta z < 7$ Å at the positive electrode and $\Delta z < 4$ Å at the negative electrode. The close approach of the cations near the negative electrode suggests [EMIM] assumes a highly aligned conformation with respect to the surface, which is somewhat surprising considering it is considerably larger than [BF_4]. We again note that different ion distributions at the constant-$\Delta\Psi$ and constant-σ electrode surfaces imply a denser surface ion layer at the constant-$\Delta\Psi$ electrode.

A simple comparison of the ion density profiles indicates that constant-$\Delta\Psi$ electrodes lead to a denser surface ion layer than constant-σ electrodes. To quantify this, we have explicitly evaluated the number of ions in the surface layer per unit area, N, by simply integrating over the initial peak found in the $\rho(\Delta z)$ profile. The results of this procedure are shown in Fig. 7a for constant-$\Delta\Psi$ and constant-σ electrodes. For both electrode conditions, we find a slight tendency toward more anions than cations in the surface layer at $\langle\Psi\rangle = 0$ V, which is likely a result of the small radius of [BF_4]. With an increase in $\langle\Psi\rangle$, we see an increase in the number of anions and a decrease in the number of cations, leading to more negatively charged surface ion layer; naturally, the opposite effect is noted when decreasing potential. We note that the number of [EMIM] cations is generally large and weakly varying, changing by only $\sim$0.25 nm^{-2} across the investigated range of potential. On the other hand, [BF_4] exhibits large changes with potential, varying by $\sim$1.25 nm^{-2} from the lowest to highest surface potentials. This implies [EMIM] interacts more favorably with the surface than [BF_4].

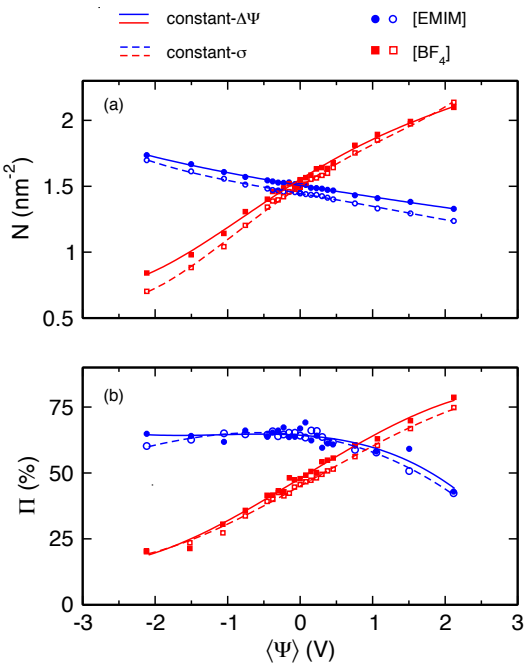

FIG. 7. Properties of the electrode surface ion layer as a function of surface potential $\langle\Psi\rangle$ for constant-$\Delta\Psi$ (solid lines) and constant-σ (dashed lines) electrodes of an $L_z = 10$ nm model capacitor. Both the (a) surface density, N, and (b) alignment with respect to the electrode surface, Π, are given for cations and anions.

Contrasting both electrode ensembles, we see that there are, indeed, more cations and anions in the surface layer at constant-$\Delta\Psi$ electrodes than the one at constant-σ electrodes. At the largest magnitude of surface potential, $|\pm 2.1|$ V, the ion density is on the order of 10-20% higher at constant-$\Delta\Psi$ electrodes. Correlating this observation with the previously noted differences in C_{dl}, we suggest that the energetic favorability of having more of both ionic species in the surface ion layer on constant-$\Delta\Psi$ electrodes makes their separation, and thus the polarization of the electrode, more difficult. Essentially, this suggests that to obtain a given value of σ requires larger potentials on constant-$\Delta\Psi$ electrodes than on constant-σ electrodes. This is consistent with the larger values of C_{dl} at low potentials on constant-σ electrodes and larger values at high potentials on constant-$\Delta\Psi$ electrodes. The average capacitance on both electrodes are practically identical because the charge accumulation attributed to higher capacitances at low potentials obtained from constant-σ electrodes is essentially spread over a larger potential range in the case of constant-$\Delta\Psi$ electrodes.

In addition to surface ion density, we also compute the potential-dependent ion configuration at the electrode surface. The possible alignments are shown in Fig. S5 of the supplemental material,[59] with [EMIM] having a

planar configuration, where the charge center is highly exposed to the surface, and a perpendicular configuration, where the interactions are primarily with the chain and the charge center is more removed from the surface. Similarly, $[BF_4]$ can assume highly interacting configurations with three F atoms close to the surface and others with fewer F atoms, one or two, in proximity to the surface. We define the percent of highly interacting planar [EMIM] cations and $[BF_4]$ having three F atoms near the surface with Π. The value of Π is determined from the angular distribution of the ring normal in [EMIM] or the B-F bond in $[BF_4]$ with respect to the electrode surface. Values of Π as a function of surface potential for constant-$\Delta\Psi$ and constant-σ surfaces are given in Fig. 7b.

The value of Π is also influenced by electrode ensemble, with constant-$\Delta\Psi$ electrodes leading to a higher value of Π for $[BF_4]$ at $\langle\Psi\rangle > 0$ V than constant-σ electrodes. The higher level of alignment of $[BF_4]$ with the electrode surface, and thus more compact packing, naturally accompanies the higher density noted at constant-$\Delta\Psi$ electrodes. There is no apparent, systematic difference in the value of Π for [EMIM] between the two electrodes, though alignment appears to be higher at positive potentials for constant-$\Delta\Psi$ electrodes when compared to constant-σ electrodes. These trends are consistent with interactions of surface ions being more favorable with constant-$\Delta\Psi$ electrodes than constant-σ electrodes, which leads to more ion alignment at the surface. This further adds veracity to the argument that a higher density, and thus more aligned, neutral surface ion layer on constant-$\Delta\Psi$ electrodes resists the formation of an EDL at low values of $\Delta\Psi$. This washes out the marked camel-type C_{dl} profile that result from surface ions being less strongly bound, and thus having a lower $\Delta\Psi$ barrier to ion segregation and EDL formation, on constant-σ electrodes.

Common to both electrode ensembles, the alignment of $[BF_4]$ shows a strong dependence on $\langle\Psi\rangle$, with Π increasing from ∼25% to ∼75% across the 4.2 V potential range. At neutral surfaces, [EMIM] cations predominantly assume the highly interacting planar configuration at the electrode surface, having Π of ∼70 %. The value of Π for [EMIM] changes little as potential decreases, suggesting the surface is saturated with planar cations even at neutral conditions. Such a fact agrees with the previous observation of a closely packed surface ion layer at the negative electrode. At the positive electrode, the value of Π for [EMIM] decreases, reaching 42% at a surface potential of 2.1 V. Overall, this agrees with the previous assertion, based on the behavior of N in Fig. 7a, that [EMIM] has more conformational freedom at the electrode surface than $[BF_4]$. Planar conformations of [EMIM] can exist at the negative electrode through chain interacting configurations where the charge center is moved form the surface.

D. Electrolyte Polarizability

The inclusion of atomic polarizability into interatomic potentials has been shown to be important to accurately represent the dynamics of ionic liquids. Ionic liquid EDLs, on the other hand, are commonly studied through non-polarizable potentials, and the effect of polarization on such interfaces has not been systematically characterized. As an initial means of understanding the influence of polarization on EDL properties, we have computed the average induced dipole moment perpendicular to the electrode surface (μ_z) as obtained from constant-$\Delta\Psi$ simulations where $\Delta\Psi = 0$ V, given in Fig. 8a. The value of μ_z is provided as a function of distance from the electrode, Δz. Negative and positive values of μ_z imply atomic dipoles pointing toward and away from the surface, respectively. The μ_z profile shares similarities with the ion density profile, shown in Fig. S4, specifically in that the atomic dipoles oscillate with the same period in Δz as ρ. The resulting oscillations dampen to $\mu_z \sim 0$ after the first few ion layers, which can be seen from a comparison with ρ in Fig. S4.

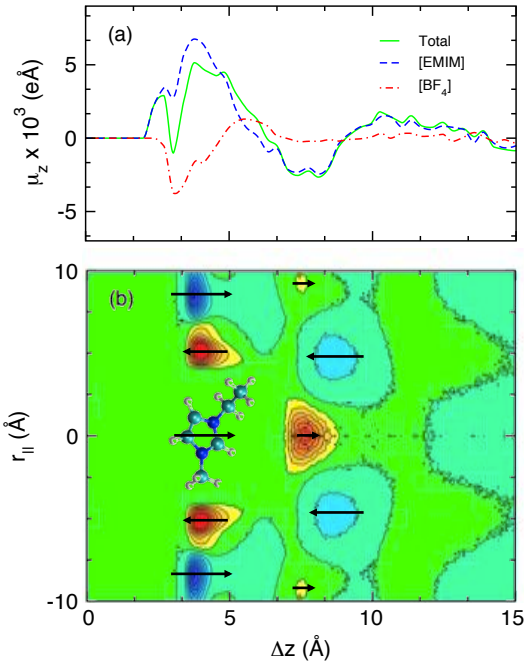

FIG. 8. Comparison of (a) the average induced dipole normal to the electrode, μ_z, for [EMIM] and $[BF_4]$ and (b) the net ion distribution, $\Delta g = g^{\text{cations}} - g^{\text{anions}}$, as a function of distance from a surface cation in the $r_{\|}$ direction and the electrode surface, Δz. Results are shown for our $L_z = 10$ nm model capacitor having $\Delta\Psi = 0$ V. More cation concentration is represented by blue regions while anion concentration is represented by red regions. The direction of the average induced dipole in a given accumulation of ions is indicated by black arrows.

The ion resolved induced dipole moments at $\Delta\Psi = 0$ V, again provided in Fig. 8 a, further show surface

cations to have dipoles directed away from the electrode, while surface anion induced dipoles are directed toward the electrode. As such, the induced dipoles are energetically unfavorable to EDL formation. For instance, at negative values of $\langle\Psi\rangle$, there is an electric field directed toward the electrode. While this attracts cations, it opposes the cation dipole moment, which is directed away from the electrode. The same mechanism is also at play for anions. Thus, the induced dipoles will soften the electrostatic interaction between the surface ion layer and the electrode surface. For instance, as the electrode becomes negatively charged, the electric field originating from the electrode opposes the alignment of induced dipoles on cations, while it is aligned with the induced dipoles of anions. This leads to a lower and higher interaction between the negative electrode with cations and anions, respectively. A similar behavior is noted as the electrode becomes positively charged, with cations being less repulsed and anions being less attracted to the electrode surface. The net effect of induced dipoles, then, is to create an energetic barrier to EDL formation.

We rationalize the behavior of the induced dipoles through an analysis of surface structure using a $r_\parallel$ and z dependent net ion distribution function, $\Delta g(r_\parallel, \Delta z)$, for surface cations, given in Fig. 8b. (The value of $\Delta g(r_\parallel, \Delta z)$ is computed as the difference between the cation and anion distribution surrounding surface cations, where the distribution is converted to distance from the cation in the $r_\parallel$ direction and from the electrode surface in the z direction for ease of comparison with the z-dependent induced dipole profile.) In effect this provides a map of ion probability as a function of distance from a surface cation, with a net cation accumulation represented by blue regions and net anion accumulation represented by red regions. Within the surface layer of ions, which occurs as $\Delta z < 5$ Å, we see surface anions at $r_\parallel = \pm 5$ Å crowding the surface cation at $r_\parallel = 0$ Å. Beyond these surface anions are aggregations of cations occurring at $r_\parallel = \pm 8$ Å, which suggests electrostatic ordering at the surface. Interestingly, the second molecular layer, occurring at 5 Å $< \Delta z <$ 10 Å shows correlation with the surface ions. Specifically, for a surface ion at a given $r_\parallel$, we see a corresponding accumulation of counterions at the same $r_\parallel$ in the second layer. This is in agreement with the noted induced dipoles, surface cations have dipoles which point away from the surface toward their correlated anions in the second layer, while surface anions point toward the surface and away from their correlated cations in the second layer. This further underlines the three-dimensional nature of the EDL.

To further elucidate the implications of the induced dipoles, we have performed a suite of simulations in the constant-$\Delta\Psi$ ensemble using the APPLE&P electrolyte potential without atomic polarization. From these simulations, we have computed the difference in capacitance between polarized and non-polarized computations, given by δC_{dl} and shown in Fig. 9 a. We see negative regions of δC_{dl} around ±0.5 V and positive region for 1 V $< \langle\Psi\rangle <$ -1 V. Overall, this leads to a net decrease in capacitance. The regions of negative δC_{dl} occur where highly resolved maxima in C_{dl} were noted for constant-σ electrodes. Having higher capacity at lower surface potentials suggests less resistance in the non-polarizable force field to formation of the EDL.

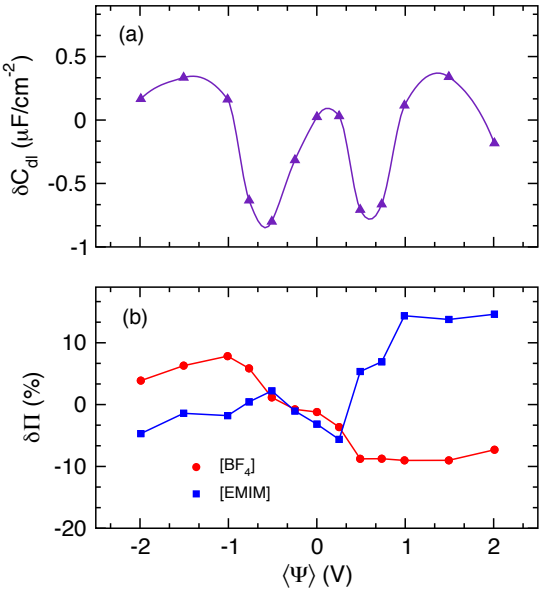

FIG. 9. Potential dependent influence of electrolyte polarization on (a) differential capacitance (δC_{dl}) and (b) surface ion alignment ($\delta\Pi$) for a $L_z = 10$ nm model capacitor using the constant-$\Delta\Psi$ formalism.

To evaluate the structural origins of the trends in δC_{dl}, we compute the difference in surface ion alignment, $\delta\Pi$, between polarized and non-polarized simulations, as given in Fig. 9 b. We see significant differences in surface ion alignment, with the anion layer at the positive electrode showing 10% lower alignment, which allows the incorporation of more cations into the surface and results in a 10-15% increase in alignment of cations at the positive electrode. A similar trend, though less marked, is seen at the negative electrode. The alignment of surface cations is decreased by up to 5%, while anions are 5-10% more aligned with the surface. The relatively small change in the value of Π for [EMIM] at the negative electrode is an additional indication that the surface is saturated with planar cations, which was previously suggested from the small changes in [EMIM] density and configuration in the polarizable system (see Fig. 7). The increased degree of configurational disorder in the polarizable EDL corresponds to the noted negative regions of δC_{dl} at relatively low potentials, which as previously noted results from the induced dipole softening of electrostatic interactions with the electrode.

IV. CONCLUSIONS

The present work is an investigation of various approaches for the MD modeling of ionic liquid EDLs. The system of focus is a model capacitor of slab-like geometry that is composed of two graphite electrodes interfaced with a polarizable electrolyte, [EMIM][BF_4]. On this system, we have quantified the influence of electrostatic summation technique, the method of charging the electrode, and the electrolyte atomic polarizability on the EDL structure and differential capacitance. Furthermore, we have compared and contrasted different methods of computing differential capacitance.

To ensure the validity of our model capacitor, we have evaluated the interplay between electrostatic summation and the assumption of quasi-2D system geometry. In this regard, our model capacitor should conform to the classical, quasi-2D parallel plate capacitor and have no electric field external to the electrodes. We find both the 3D Ewald summation corrected for slab geometry and the more expensive, though exact, 2D Ewald summation yield model capacitors that are effectively quasi-2D. Alternatively, the use of an uncorrected 3D Ewald summation is not compatible with quasi-2D geometry, which leads to errors in the electrode potential and charge.

We have additionally investigated how different techniques for charging the electrode, namely constant-$\Delta\Psi$ and constant-σ ensembles, influence differential capacitance. To efficiently perform this analysis, we derive fluctuation expressions for C_{dl} for both constant-$\Delta\Psi$ ($C_{\Delta\Psi}$) and constant-σ (C_σ) ensembles. These expressions provide differential capacitance on a *per* electrode basis and are validated through a comparison to the direct derivative of σ with respect to Ψ. Differential capacitance computations performed for both constant-$\Delta\Psi$ and constant-σ electrodes show differences in overall shape, but provide similar averages over $-2\text{ V} < \langle\Psi\rangle < 2\text{ V}$. Constant-$\sigma$ electrodes produce capacitance profiles with highly resolved peaks conforming to the camel-shaped profile, while constant-$\Delta\Psi$ electrodes yield a capacitance that is more diffuse and does not as clearly exhibit camel-type character.

The differences in C_{dl} with respect to electrode ensemble originate in the behavior of the surface ion layer, or Stern layer. An analysis of the $\langle\Psi\rangle$-dependent density of this layer shows more ions, both cations and anions, are present at the constant-$\Delta\Psi$ electrode than at the constant-σ electrode. Such an effect likely arises from the variable surface charge on the constant-$\Delta\Psi$ electrode, which, unlike the constant-σ approach, responds to surface ions to create a more favorable electrostatic interaction. The denser surface ion layer on constant-$\Delta\Psi$ electrodes, then, requires a higher value of $\langle\Psi\rangle$ to achieve the same polarization as the layer on the constant-σ electrode. Thus, large values of C_{dl} present between $-0.75\text{ V} < \langle\Psi\rangle < 0.75\text{ V}$ on constant-σ electrodes are distributed over a larger potential range on constant-$\Delta\Psi$ electrodes, leading to a more diffuse profile with lower maximum values of Cdl.

The role of electrolyte polarization has been analyzed through comparisons with non-polarizable electrolyte models on constant-$\Delta\Psi$ electrodes. We find that the average value of capacitance increases slightly and that the camel shaped profile becomes more resolved when polarization is removed. This effect has been related the fact that induced dipoles oppose the field generated by the electrode, thereby softening the electrostatic interaction between ions and the electrified surface. This can be further traced to ion correlation effects between surface ions and those in the second layer, which underscore the three dimensional nature of the EDL. For charged electrodes, there is a competition between the electrode surface charge and the second molecular layer, whose electric fields oppose, to determine the direction of induced dipoles on the surface ions.

We have shown, then, how details of MD simulation can affect the resulting $\langle\Psi\rangle$-dependent profile of C_{dl}. Our results suggest that simpler models, such as electrolytes interacting through charge alone and surfaces having a constant σ, lead to highly idealized camel-type differential capacitance profiles that more clearly reflect the predictions of mean field models of ionic liquid behavior at ideal metallic electrodes. As additional atomic detail is incorporated into the simulation, such as electrolyte polarization and charge redistribution on the electrode surface, the $\langle\Psi\rangle$-dependent profile of C_{dl} becomes more complex and, in our case, loses some of its camel-type character. This reflects the sensitive balance of forces that influence the density and configuration of ions in the Stern layer and underscores potential challenges in comparing the experimentally obtained values of capacitance with those obtained from theory.

ACKNOWLEDGMENTS

This work was supported by funding from the NASA Aeronautics Research Institute Seedling program.

[1] V. Lockett, R. Sedev, J. Ralston, M. Horne, and T. Rodopoulos, J. Phys. Chem. C **112**, 7486 (2008).
[2] M. M. Islam, M. T. Alam, and T. Ohsaka, J. Phys. Chem. C **112**, 16568 (2008).
[3] V. Lockett, M. Horne, R. Sedev, T. Rodopoulos, and J. Ralston, Phys. Chem. Chem. Phys. **12**, 12499 (2010).
[4] T. Pajkossy and D. M. Kolb, Electrochim. Commun. **13**, 284 (2011).
[5] M. Gnahm, T. Pajkossy, and D. M. Kolb, Electrochim. Acta **55**, 6212 (2010).
[6] J. P. Zheng, P. C. Goonetilleke, C. M. Pettit, and D. Roy, Talanta **81**, 1045 (2010).
[7] J. Zheng, S. S. Moganty, P. C. Goonetilleke, R. E. Baltus, and D. Roy, J. Phys. Chem. C **115**, 7527 (2011).
[8] R. M. Lynden-Bell, M. G. Del Pópolo, T. G. A. Youngs, J. Kohanoff, C. G. Hanke, J. B. Harper, and C. C. Pinilla, Acc. Chem. Res. **40**, 1138 (2007).
[9] S. Tazi, M. Salanne, C. Simon, P. Turq, M. Pounds, and P. A. Madden, J. Phys. Chem. B **114**, 8453 (2010).
[10] N. N. Rajput, J. Monk, R. Singh, and F. R. Hung, J. Phys. Chem. C **116**, 14504 (2012).

[11] C. Pinialla, M. G. Del Pópolo, J. Kohanoff, and R. M. Lynden-Bell, J. Phys. Chem. B **111**, 4877 (2007).
[12] P. Wu, J. Huang, V. Meunier, B. G. Sumpter, and R. Qiao, ACS Nano **5**, 9044 (2011).
[13] G. Feng and P. T. Cummings, J. Phys. Chem. Lett. **2**, 2859 (2011).
[14] Y. Shim and H. J. Kim, ACS Nano **4**, 2345 (2010).
[15] C. Merlet, B. Rotenberg, P. A. Madden, P.-L. Taberna, P. Simon, Y. Gogotsi, and M. Salanne, Nature Mater. **11**, 306 (2012).
[16] D. Jiang, Z. Jin, and J. Wu, Nano Lett. **11**, 5373 (2011).
[17] G. Feng, R. Qiao, J. Huang, B. G. Sumpter, and V. Meunier, J. Phys. Chem. C **114**, 18012 (2010).
[18] S. Li, K. L. Van Aken, J. K. McDonough, G. Feng, Y. Gogotsi, and P. T. Cummings, J. Phys. Chem. C **118**, 3901 (2014).
[19] M. V. Fedorov and A. A. Kornyshev, J. Phys. Chem. B **112**, 11868 (2008).
[20] G. Feng, J. S. Zhang, and R. Qiao, J. Phys. Chem. C **113**, 4549 (2009).
[21] Y. Shim, Y. Jung, and H. J. Kim, J. Phys. Chem. C **115**, 23574 (2011).
[22] Z. Hu, J. Vatamanu, O. Borodin, and D. Bedrov, Electrochim. Acta **145**, 40 (2014).
[23] J. Vatamanu, M. Vatamanu, and D. Bedrov, ACS Nano **Just Accepted**, Just Accepted (2015).
[24] J. Vatamanu, O. Borodin, and G. D. Smith, J. Am. Chem. Soc. **132**, 14825 (2010).
[25] J. Vatamanu, O. Borodin, and G. D. Smith, J. Phys. Chem. B **115**, 3073 (2011).
[26] D. Bedrov, J. Vatamanu, and Z. Hu, J. Non-Cryst. Solids , in press (2014).
[27] J. Vatamanu, O. Borodin, and G. D. Smith, Phys. Chem. Chem. Phys. **12**, 170 (2010).
[28] J. Vatamanu, O. Borodin, and G. D. Smith, J. Phys. Chem. C **116**, 1114 (2011).
[29] K. Breitsprecher, K. Szuttor, and C. Holm, J. Phys. Chem. C **119**, 22445 (2015).
[30] C. Merlet, M. Salanne, B. Rotenberg, and P. A. Madden, J. Phys. Chem. C **115**, 16613 (2011).
[31] C. Merlet, D. Limmer, M. Salanne, R. van Roij, P. A. Madden, D. Chandler, and B. Rotenberg, J. Phys. Chem. C **118**, 18291 (2014).
[32] N. N. Rajput, J. Monk, R. Singh, and F. R. Hung, J. Phys. Chem. C **116**, 5169 (2012).
[33] K. L. Van Aken, J. K. McDonough, S. Li, G. Feng, S. M. Chathoth, E. Mamontov, P. F. Fulvio, P. T. Cummings, S. Dai, and Y. Gogotsi, J. Phys.: Condens. Matter **26**, 284104 (2014).
[34] J. B. Haskins, W. R. Bennett, J. J. Wu, D. M. Hernández, O. Borodin, J. D. Monk, C. W. Bauschlicher Jr., and J. W. Lawson, J. Phys. Chem. B **118**, 11295 (2014).
[35] O. Borodin, S. G. D., and W. Henderson, J. Phys. Chem. B **110**, 16879 (2006).
[36] Z. Li, G. D. Smith, and D. Bedrov, J. Phys. Chem. B **116**, 12801 (2012).
[37] C. J. F. Solano, S. Jeremias, E. Paillard, D. Beljonne, and R. Lazzaroni, J. Chem. Phys. **139**, 034502 (2013).
[38] J. B. Haskins, C. W. Bauschlicher Jr., and J. W. Lawson, J. Phys. Chem. B **119**, 14705 (2015).
[39] C. W. Bauschlicher Jr., J. B. Haskins, E. W. Bucholz, J. W. Lawson, and O. Borodin, J. Phys. Chem. B **118**, 10785 (2014).
[40] M. V. Fedorov and A. A. Kornyshev, Chem. Rev. **114**, 2978 (2014).
[41] J. M. Black, D. Walters, A. Labuda, G. Feng, P. C. Hillesheim, S. Dai, P. T. Cummings, S. V. Kalinin, R. Proksch, and N. Balke, Nano Lett. **13**, 5954 (2013).
[42] J. I. Siepmann and M. Sprik, J. Chem. Phys. **102**, 511 (1995).
[43] M. Sprik and M. L. Klein, J. Chem. Phys. **89**, 7556 (1988).
[44] M. Kawata and M. Mikami, Chem. Phys. Lett. **340**, 157 (2001).
[45] I.-C. Yeh and M. L. Berkowitz, J. Chem. Phys. **111**, 3155 (1999).
[46] D. T. Limmer, C. Merlet, M. Salanne, D. Chandler, P. A. Madden, R. van Roij, and B. Rotenberg, Phys. Rev. Lett. **111**, 106102 (2013).
[47] Z. Wang, Y. Yang, D. L. Olmstead, M. Asta, and B. B. Laird, J. Chem. Phys. **141**, 184012 (2014).
[48] S. K. Reed, O. J. Lanning, and P. A. Madden, J. Chem. Phys. **126**, 084704 (2007).
[49] C. Merlet, C. Péan, B. Rotenberg, P. A. Madden, P. Simon, and M. Salanne, J. Phys. Chem. Lett. **4**, 264 (2013).
[50] O. Borodin and G. D. Smith, J. Phys. Chem. B **110**, 6279 (2006).
[51] O. Borodin and G. D. Smith, J. Phys. Chem. B **110**, 6293 (2006).
[52] O. Borodin, J. Phys. Chem. B **113**, 11463 (2009).
[53] D. E. Parry, Surf. Sci. **49**, 433 (1975).
[54] D. M. Heyes, M. Barber, and J. H. R. Clarke, J. Chem. Soc., Faraday Trans II **73**, 1485 (1977).
[55] S. W. de Leeuw and J. W. Perram, Mol. Phys. **37**, 1313 (1979).
[56] J. B. Haskins and J. W. Lawson, J. Phys. Chem. C **(Submitted)**.
[57] H. Nyquist, Phys. Rev. **32**, 110 (1928).
[58] J. B. Johnson, Phys. Rev. **32**, 97 (1928).
[59] See supporting information for additional details of the ion density profiles and structure at the surface.

SUPPLEMENTARY MATERIAL

Contents

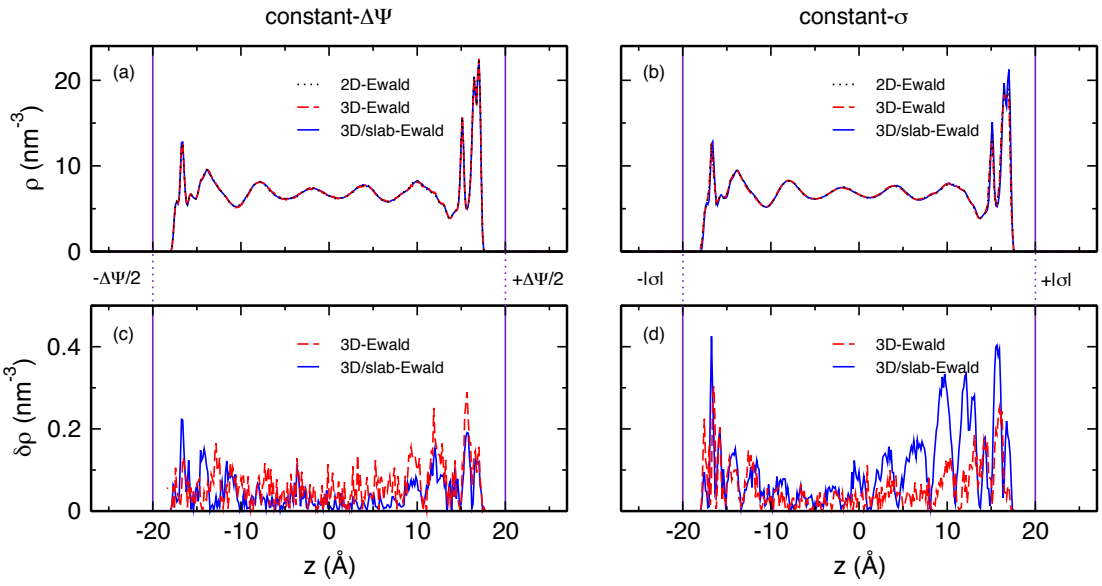

Figure S1. Influence of long-range electrostatic summation technique (2D, 3D, and 3D/slab Ewald summation) on structure. Both the (a,b) total ion density and (c,d) deviation of density obtained from simulations using the 3D and 3D/slab summation techniques from that given by the 2D Ewald summation technique are shown. The simulations are performed using (a,c) constant-$\Delta\Psi$ electrodes having a potential drop of 6 V and (b,d) constant-σ electrodes having a surface charge density of 13.18 μC/cm^2.

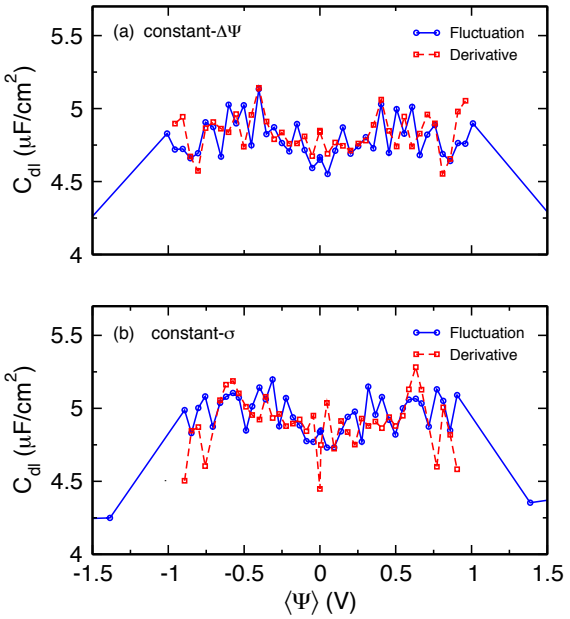

FIGURE S2. Comparison of the differential capacitance obtained from L_z systems having (a) constant-$\Delta\Psi$ and (b) constant-σ electrodes. Capacitance from both the fluctuation formulas (solid lines) as well as the numerical derivative of the charge density (dashed lines) are provided.

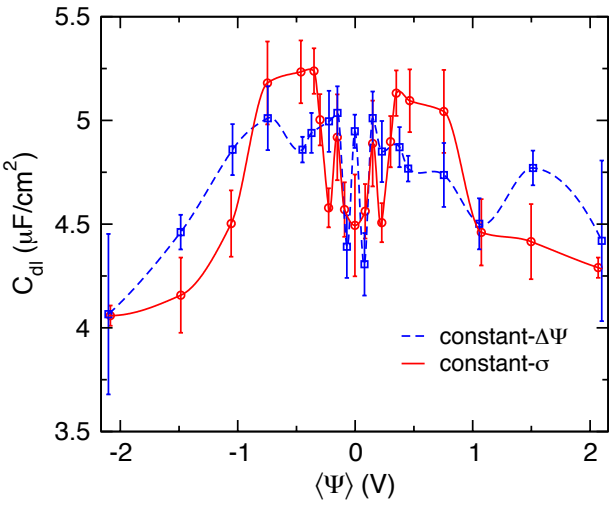

FIGURE S3. Differential capacitance of an $L_z = 10$ nm capacitor as obtained from the use of constant-$\Delta\Psi$ (dashed lines) and constant-σ (solid lines) electrodes. Error bars are obtained from the standard deviation of C_{dl} as a function of simulation time are included.

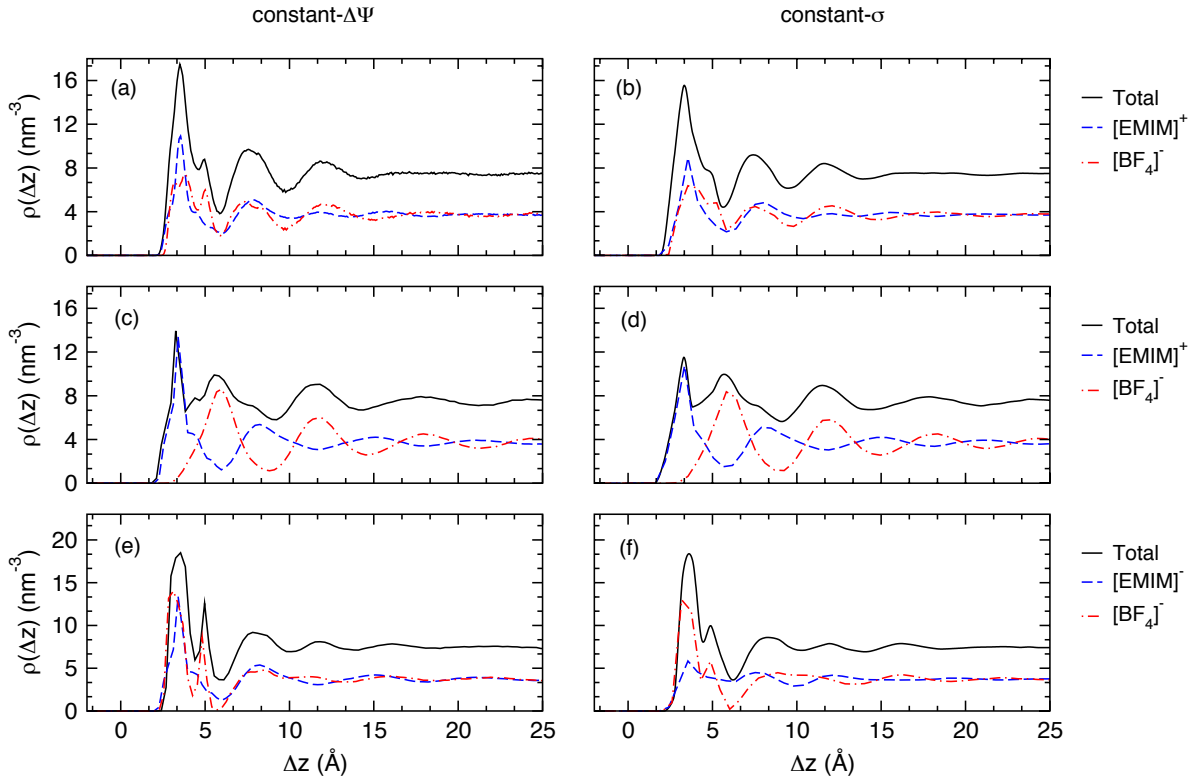

FIGURE S4. Ion density profiles as a function of distance, Δz, from (a,b) neutral, (c,d) negative, and (e,f) positive electrodes. Results are obtained using both (a,c,e) constant-$\Delta\Psi$ and (b,d,f) constant-σ conditions.

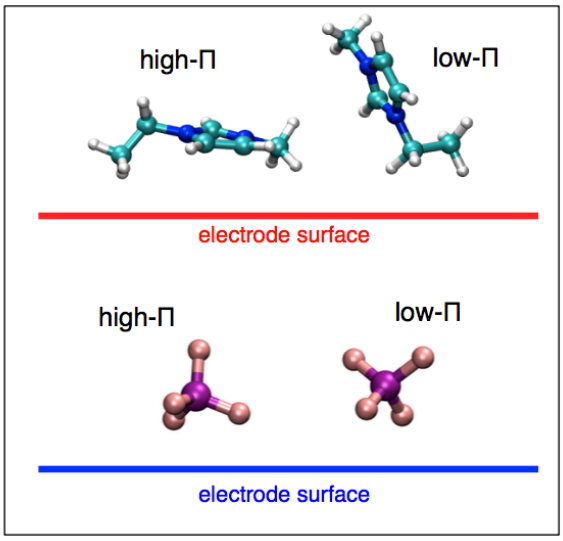

FIGURE S5. Cation and anion alignment with the electrode surface representing high and low values of Π.